



# DEM simulation of the packing of cylindrical particles

Jieqing Gan<sup>1</sup> · Aibing Yu<sup>1</sup>

Received: 22 February 2019 / Published online: 8 January 2020  
© Springer-Verlag GmbH Germany, part of Springer Nature 2020

## Abstract

Discrete element method is used to study the effect of particle aspect ratio on the packing structure of cylinders in this work. Two contact scenarios are complemented to detect particle contacts, following the work of Kodam et al. (Chem Eng Sci 65:5852–5862, 2010) and Guo et al. (Powder Technol 228:193–198, 2012). The results show that the packing density–aspect ratio curve has two small peaks at aspect ratio of 0.625 and 1.25, and a small cusp at aspect ratio of 1.0. Excluded volume is used to explain the variation of packing density with aspect ratio for cylinders, spherocylinders and ellipsoids. The lowest ensemble-averaged coordination number is found at aspect ratio of around 0.75. For platy cylinders, the dominant contact scenario is the face–edge contacts, followed by band–edge contacts. For elongated cylinders, the major contact scenarios are band–edge and band–band contacts. The existence of the planar faces of a platy cylinder makes the radial distribution functions of disks quite different from that of smooth-curved oblates. Most platy cylinders have their principal axis of pointing to and almost paralleling to the vertical direction, while the principal axis of elongated cylinders tends to point to the horizontal plane. The platy particles tend to form stacks composed of 2–4 particles for different aspect ratios. The force gradient increases and force magnitude becomes less uniform when  $L/D$  deviates from 1.0.

**Keywords** Packing · Cylinders · Discrete element method · Excluded volume · Contact detection

## 1 Introduction

Packing of particles with different shapes pervades the pharmaceutical, chemical, agricultural, mining, building materials, explosives, and food industries. It has been an interesting topic for decades, and extensively studied experimentally [3, 4] or mathematically [5–9]. A number of factors, e.g., packing method, container shape/boundary conditions and particle properties, can affect the packing structure and hence transport properties. Particle shape has been identified as one of the most important particle properties.

Many efforts have been made to investigate the packing of non-spherical particles. In these studies, cylinders/disks,

spherocylinders and ellipsoids are commonly used to represent a large range of particle shape varying from platy to elongated. For example, the porosity–sphericity relationship is obtained based on the packing results of cylinders and disks by Zou and Yu [10]. Simulation and experimental studies on spherocylinders [11] and ellipsoidal packing [12–14] both showed that a small deviation in shape from spheres may change the packing density significantly. Local alignment was found in the packing of fibres [15], ellipsoids [13, 16], and bean, nail and cylinder particles [17]. These particles all experience a bias away from the vertical axis towards the horizontal direction due to the influence of gravity. Although some similarities are observed at a macroscopic scale, detailed qualitative and quantitative analyses of the packing structure are still lacking, especially for cylinders.

Different methods can be used to generate a packed bed of non-spherical particles, for example, discrete element method (DEM) [13, 14, 18], Monte Carlo (MC) [19], molecular dynamics (MD) [12, 20] or event driven molecular dynamics (EDMD) [21], mechanical contraction method (MCM) [11], and combined methods of MCM-MD [22] or MCM2 (modified MCM)-MC [23], digital packing algorithm (DigiPac)

---

This article is part of the Topical Collection: In Memoriam of Robert P. Behringer.

✉ Jieqing Gan  
jieqing.gan@monash.edu

✉ Aibing Yu  
aibing.yu@monash.edu

<sup>1</sup> ARC Research Hub for Computational Particle Technology, Department of Chemical Engineering, Monash University, Clayton, VIC 3800, Australia

[24], and relaxation algorithm [25, 26]. Among these methods, DEM and MD are dynamic simulation methods which consider the mechanical forces between particles, while the others, commonly referred to as “packing algorithms”, are geometric based packings without consideration of friction. Different techniques produce qualitatively comparable but quantitatively unequal packing densities (e.g., within 10% difference of each other). Frictionless packing describes the densest possible packing of dry, cohesionless particles, while frictional packing, often quoted as random loose packing for spheres [27], can exist over a substantial range in packing fraction. However, it is no longer “random” since ordered orientational packing structures exist for loose packing of non-spherical grains [28]. DEM simulations can provide different packing densities with varying sliding or rolling friction coefficients. The packing density results of spherocylinders generated using the geometric based relaxation algorithm by Zhao et al. [26] are noticeably higher than any other studies, such as [11, 23, 29, 30]. The MCM generates reproducible random packings of non-spherical shapes with densities that are slightly below values from EDMD [12]. However, the MCM has yielded contact numbers that are unphysical for high aspect ratio spherocylinders [22].

In recent years, discrete element method (DEM) has been increasingly used to study the packing of non-spherical particles due to its unique advantage in providing dynamic information. Different approaches to represent and model non-spherical particles, such as polygon formulation, composite particles, continuous function representation (CFR), discrete function representation (DFR) or spherocylinders, have been proposed, as summarized by Kodam et al. [1] and Lu et al. [31]. For composite particles, particularly clumping of spheres [32–35], the contact detection is simple, but composite particles tend to have bumpy surfaces, and a large number of components (spheres) will be needed to construct a given shape, resulting in a very demanding computational effort. For the CFR approach, a non-spherical particle (e.g. ellipsoids [13, 14] and superellipsoids [36, 37]) is well described by a simple equation. However, it can only be used for smooth and continuous surface particles, and the computational time for contact detection is also huge, because it involves the numerical solution of a high-order equation. For the DFR method [24], a particle surface is discrete using a sufficient number of points and the contact between particles are detected using a geometric potential energy method. The computational effort is also extraordinary if accurate and robust results are to be ensured. Other methods have also been proposed, including for example, the method based on orientation discretization database solution [38]. This method obtains the overlap information by space discretization of particles, and stores the information in a database. It is able to determine the overlap between two arbitrarily-shaped particles without the need to solve

any complicated equations. However, in the case of three-dimensional system, a huge database will be needed to facilitate a simulation.

Therefore, for a specific particle shape, for example, cylinders as concerned in the present study, none of the above contact detection algorithms is efficient. However, Kodam et al. [1] proposed detection criteria for cylinders by considering several contact scenarios between particles and between a particle and wall. Although not applicable to other particle shapes, this method is much more computational efficient. More recently, Guo et al. [2] further developed the method. These two studies lay out a good foundation for the DEM simulation of cylindrical particles.

The aim of this work is to study the packing structure of cylindrical particles using DEM. Cylinders differ from the well-studied spherocylinders and ellipsoids by the existence of the planar faces. This makes it more difficult for the contact detection and also brings difference in packing structure from the continuous surface spherocylinders and ellipsoids. In this work, the contact detection algorithms based on Kodam et al. [1] and Guo et al. [2] are further developed for platy cylinders. Then, it focuses on the effect of one single parameter for cylinders, i.e., aspect ratio (= particle length  $L$ /diameter  $D$ ) on the packing structure. The packing structure is also compared with that of spherocylinders and ellipsoids. The results are analysed in terms of the packing density [or porosity (=  $1 - \text{packing density}$ )], coordinate number, the spatial orientation and radial distribution function. The force network among particles and force distribution are also analysed.

## 2 Simulation method

### 2.1 Governing equations

According to the DEM, a particle can have two types of motion: translational and rotational, which are determined by Newton’s second law of motion. The governing equations for the translational and rotational motion of particle  $i$  with mass  $m_i$ , and moment of inertia  $I_i$  can be written as

$$m_i \frac{d\mathbf{v}_i}{dt} = \sum_{j=1}^{k_c} (\mathbf{f}_{ij}) + m_i \mathbf{g} \quad (1)$$

and

$$I_i \frac{d\boldsymbol{\omega}_i}{dt} = \sum_{j=1}^{k_c} (\mathbf{M}_{r,ij} + \mathbf{M}_{r,ij} + \mathbf{M}_{n,ij}) \quad (2)$$

where  $\mathbf{v}_i$  and  $\boldsymbol{\omega}_i$  are the translational and angular velocities of the particle at the centre of mass, respectively, and  $k_c$  is the number of particles in interaction with the particle.

The translational movement of the particle of mass  $m_i$  is driven by the resultant contact force  $\mathbf{f}_i$ , and the particle rotation is induced by the torque  $\mathbf{M}_i$  arising from the contact forces. The forces involved are: the gravitational force  $m_i\mathbf{g}$ , and interparticle forces  $\mathbf{f}_{ij}$  between particles  $i$  and  $j$ . These interparticle forces  $\mathbf{f}_{ij}$  can be resolved into the normal  $\mathbf{f}_{n,ij}$  and tangential  $\mathbf{f}_{t,ij}$  components at a contact point. The torque acting on particle  $i$  by particle  $j$  includes two components:  $\mathbf{M}_{t,ij}$  which is generated by the tangential force and causes particle  $i$  to rotate, and  $\mathbf{M}_{r,ij}$ , commonly known as the rolling friction torque [39], is generated by asymmetric normal forces and slows down the relative rotation between particles. For non-spherical particles, addition torque  $\mathbf{M}_{n,ij}$  should be added because the normal contact forces do not necessarily pass through the particle centre. Moreover, particle may undergo multiple interactions, so the individual interaction forces and torques are summed over the  $k_c$  particles interacting with particle  $i$ .

## 2.2 Particle–particle interaction forces

DEM has been applied to cylindrical particles by a few researchers [34, 35, 40]. As interaction forces and particle displacements are both dependent on the chosen contact model, in this work, the popular Hertz-Mindlin contact model is used. The Hertz-Mindlin contact model computes the normal contact forces  $\mathbf{f}_{n,ij}$  in a similar way to Tsuji et al. [41]. Thus, the contact force in the normal direction is given by

$$\mathbf{f}_{n,ij} = \min\left(0, k_{n,ij}\delta_{n,ij} - 2\mu_n\sqrt{m_{ij}k_{n,ij}v_{n,ij}}\right) \quad (3)$$

where  $k_{n,ij}$  is the normal stiffness,  $\delta_{n,ij}$  is the normal overlap,  $\mu_n$  is the normal damping coefficient,  $v_n$  is the normal relative velocity,  $m_{ij}$  is the effective mass given by  $1/m_{ij} = 1/m_i + 1/m_j$  and  $k_{n,ij}$  is the effective normal stiffness defined as  $1/k_{n,ij} = 1/k_{n,i} + 1/k_{n,j}$ . The stiffness of contact is sometimes directly adjustable in some DEM codes, but most DEM codes derive the stiffness of contact from the properties of the material and colliding particles. For example, the stiffness of the Hertz-Mindlin model is given by:  $k_{n,ij} = 4E_{ij}\sqrt{R_{ij}}/3$ , where  $E_{ij}$  is the effective Young's modulus and  $R_{ij}$  is the effective particle radius given by  $1/R_{ij} = 1/R_i + 1/R_j$ . For cylindrical particles,  $R_i$  and  $R_j$  represent the radii of the circular end faces of two cylinders in contact [42].

In the tangential direction, the friction force is modelled as a damped linear spring, and its magnitude is limited by Coulomb's law, such that:

$$\mathbf{f}_{t,ij} = \min\left(\mu_s k_{n,ij}\delta_{n,ij}, k_{t,ij}\delta_{t,ij} - 2\mu_t\sqrt{m_{ij}k_{t,ij}v_{t,ij}}\right) \quad (4)$$

where  $\mu_s$  is the coefficient of sliding friction,  $\mu_t$  is the damping factor in the tangential direction, and  $v_{t,ij}$  is the relative

velocity in the tangential direction. The tangential displacement  $\delta_{t,ij}$  is calculated according to  $\delta_{t,ij} = \int v_{t,ij} dt$  and the effective tangential stiffness is defined as  $1/k_{t,ij} = 1/k_{t,i} + 1/k_{t,j}$ .

Rolling friction by the Hertz-Mindlin contact model on cylindrical particles is calculated by applying torque to the contacting surfaces. The rolling friction torque is expressed by

$$\mathbf{M}_{r,ij} = \mu_r |\mathbf{f}_{n,ij}| r_i \hat{\boldsymbol{\omega}}_{t,ij} \quad (5)$$

where  $\mu_r$  is the coefficient of rolling friction,  $r_i$  is the distance of contact point from the centre of mass and  $\hat{\boldsymbol{\omega}}_{t,ij}$  is the unit angular velocity vector of the particle at the contact point. The moment calculated due to the rolling resistance is added to the total moment acting on the particle.

## 2.3 Contact detection and particle orientation

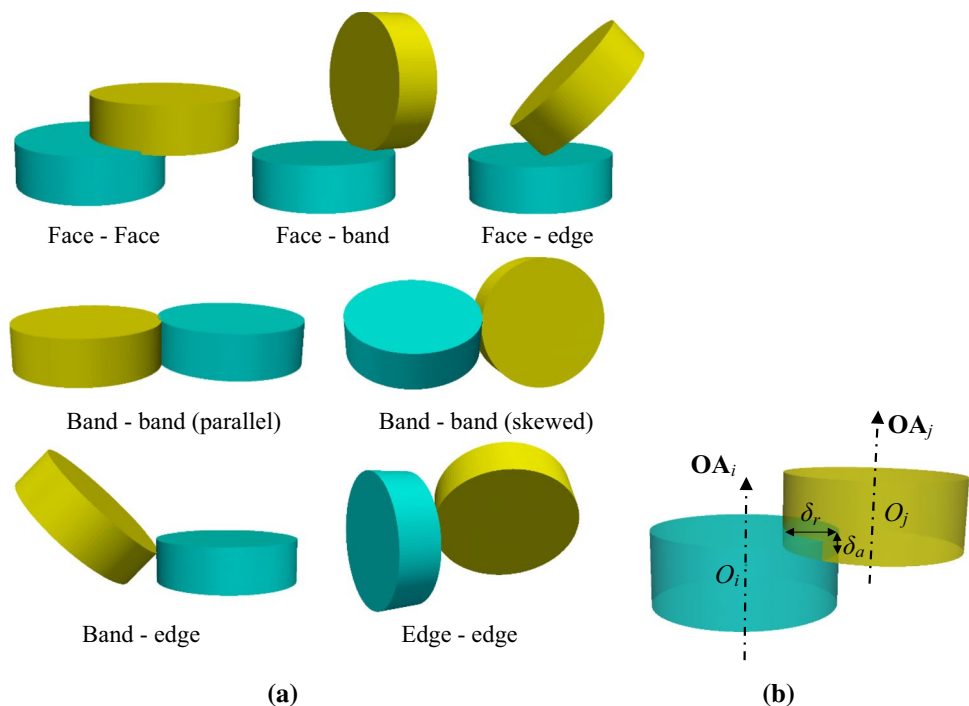
### 2.3.1 Contact detection

A cylinder consists of three parts as shown in Fig. 1: the cylinder faces (the two flat portions), the cylinder band, and the (two) edges between the faces and band. The size of the cylinder is characterized by the band radius,  $R$  (or diameter,  $D$ ), and the face-to-face length,  $L$ . A body-fixed frame of reference is located at the centre of the cylinder with the local  $z$ -axis oriented along the cylinder's axial direction. The location of the cylinder in the global frame of reference (denoted by the superscript "G") is given as  $\mathbf{x}^G$ , while the orientation is described by the unit vector aligned with the cylinder's body-fixed  $z$  axis  $\mathbf{e}_z^i$ .  $x_j^i$ ,  $y_j^i$  and  $z_j^i$  are the  $x$ ,  $y$ , and  $z$  components of cylinder  $j$ 's position in cylinder  $i$ 's body-fixed frame of reference. The bold symbols denote the vectors.

For a cylinder-flat plane interaction, three potential contact scenarios are possible: a face-plane contact, a band-plane contact, and an edge-plane contact [1]. For a cylinder–cylinder interaction, six primary contact scenarios [1, 2] (as illustrated in Fig. 1a) are possible: face–face, face–band, face–edge, band–band (parallel and skewed), band–edge, and edge–edge. The contact criteria and parameters describing the contact, i.e. the contact overlap,  $\delta_c$ , the contact location,  $\mathbf{P}_c$ , and the unit normal vector for the contact,  $\mathbf{n}_c$  can be obtained. The axial overlap  $\delta_a$  is given by  $\delta_a = \frac{1}{2}(L_i + L_j) - |z_j^i|$ , while the radial overlap  $\delta_r$  is given by  $\delta_r = (R_i + R_j) - \sqrt{(x_j^i)^2 + (y_j^i)^2}$ .

Kodam et al. [1] proposed detection criteria for different contact scenarios. However, as shown in Fig. 1b, there is another contact scenario between the face–edge and band–edge scenarios, where the radial overlap  $\delta_r$  is greater than the axial overlap  $\delta_a$ . Guo et al. [2] added this scenario

**Fig. 1** **a** Contact scenarios between two cylinders proposed by Kodam et al. [1] and **b** an additional contact scenario proposed by Guo et al. [2] (Note:  $OA_i$  is not parallel to  $OA_j$ )



as a special contact scenario and proposed a detection criterion for it. Besides, Guo et al. [2] also slightly modified the detection criterion for face–edge and band–edge contacts. In Fig. 1b, the principal axes  $OA$  of particle  $i$  and  $j$  are also shown ( $OA_i$  is not parallel to  $OA_j$ ). Table 1 summarizes the contact scenarios and the corresponding detection criteria based on Kodam et al. [1] and Guo et al. [2].

However, there are still some contact scenarios not able to be detected. For example, as shown in Fig. 2a, for very platy cylinders, both edges of particle  $j$  may contact with one edge of particle  $i$ , and this case cannot be detected as the band–band, face–edge, band–edge, or edge–edge contact according to the detection criteria proposed by Kodam et al. [1] and Guo et al. [2]. For disks, the more computationally expensive glued sphere method is used. Here we proposed a method to overcome this problem. We label the deepest point from cylinder  $j$  to cylinder  $i$  and lies within cylinder  $i$  as point  $\mathbf{P}_d$ . According to the positions of contact points  $\mathbf{A1}$ ,  $\mathbf{B1}$  and  $\mathbf{A2}$ ,  $\mathbf{B2}$  (see the “Appendix” for the calculation of these points), the position of  $\mathbf{P}_d$  is calculated as the centre point on the band of cylinder  $j$  of these 4 points. Thus, the axial overlap  $\delta_a$  and radial overlap  $\delta_r$  can be calculated according to the position of point  $\mathbf{P}_d$ . For this case, the contact points and normal vectors can be decided according to the band–edge criteria proposed by Kodam et al. [1] or the corrected criteria for the special contact by Guo et al. [2] as given in Table 1.

Another contact scenario is shown in Fig. 2b. When the two edges of particle  $j$  cross the two edges of particle

$i$ , it cannot be detected according to the criterion of band–band contact. This is because the contact location of  $l_i^*$  or  $l_j^*$  does not lie within the length of each cylinder (Note that  $l_i^*$  and  $l_j^*$  are the shortest distance line between the cylinders intersecting the two cylinder axes at points defined by Vega and Lago [43]). The calculation of  $l_i^*$  and  $l_j^*$  are given in Table 1). To overcome this problem, the closest point  $\mathbf{P}_c$  is here calculated as the centre point on the band of cylinder  $j$  of the closest points  $\mathbf{P1}$  and  $\mathbf{P2}$ . The axial overlap  $\delta_a$  and radial overlap  $\delta_r$  can be calculated according to the position of point  $\mathbf{P}_c$ . For this case, the contact points and normal vector can also be treated in a similar way to the band–edge contact by Kodam et al. [1] as given in Table 1.

### 2.3.2 Particle orientation

For three-dimensional particles, the moments of inertia  $I_i$  must be calculated in every time step according to the new orientation of the particle in the space. For spherical particles,  $I_{1i}=I_{2i}=I_{3i}=I_i$  and body-fixed coordinates can be set in the same direction as space-fixed ones. For non-spherical particles, the local and global orientation of a particle can be transformed using the space-fixed and body-fixed coordinate systems. The space-fixed coordinate system is fixed with respect to the laboratory space. On the other hand, the body-fixed (or local) coordinate system is a moving Cartesian coordinate system, which is fixed with respect to the

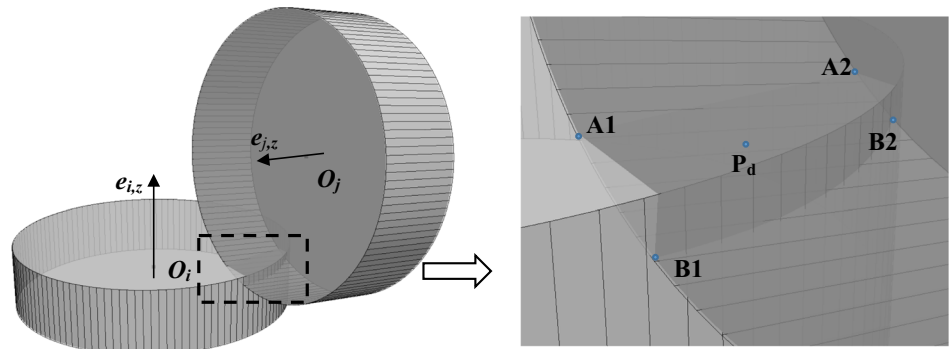
**Table 1** Contact detection criteria for different contact scenarios proposed by Kodam et al. [1] and corrected by Guo et al. [2]

Contact scenarios	Contact detection criteria proposed by Kodam et al. [1]	Contact detection criteria corrected by Guo et al. [2]
Face–face	if $\left\{ \begin{array}{l} \left( \left  \mathbf{e}_{i,z}^G \cdot \mathbf{e}_{j,z}^G \right  = 1 \right) \text{ and} \\ \left[ \left  z_j^i \right  < \frac{1}{2} (L_i + L_j) \right] \text{ and} \\ \left[ (x_j^i)^2 + (y_j^i)^2 < (R_i + R_j)^2 \right] \end{array} \right\}$ , then contact occurs	
Face–band	if $\left\{ \begin{array}{l} \left( \left  \mathbf{e}_{i,z}^G \cdot \mathbf{e}_{j,z}^G \right  = 0 \right) \text{ and} \\ \left[ \left  z_j^i \right  < \left( \frac{1}{2} L_i + R_j \right) \right] \text{ and} \\ \left[ S < \left( \frac{1}{2} L_j + R_j \right) \right] \text{ and} \\ t < t^* \end{array} \right\}$ , then contact occurs where $S = \left  \mathbf{x}_j^i \cdot \mathbf{e}_{j,z}^i \right $ , $t = \sqrt{(x_j^i)^2 + (y_j^i)^2 - S^2}$ , $t^* = \begin{cases} R_i, & \text{if } S < \left( \frac{1}{2} L_j \right) \\ \sqrt{R_i^2 - \left( S - \frac{1}{2} L_j \right)^2}, & \text{otherwise.} \end{cases}$	
Face–edge	if $\left\{ \begin{array}{l} \left[ \left  z_E^i \right  < \frac{1}{2} L_i \right] \text{ and} \\ \left[ (x_E^i)^2 + (y_E^i)^2 < R_i^2 \right] \text{ and} \\ \left[ \left( \frac{1}{2} L_i - \left  z_E^i \right  \right) < R_i - \sqrt{(x_E^i)^2 + (y_E^i)^2} \right] \text{ and} \\ \left[ \left  z_j^i \right  > \frac{1}{2} L_i \right] \end{array} \right\}$	if $\left\{ \begin{array}{l} \left[ \left  z_E^i \right  < \frac{1}{2} L_i \right] \text{ and} \\ \left[ (x_E^i)^2 + (y_E^i)^2 < R_i^2 \right] \text{ and} \\ \left[ \overline{EO}_i \cdot \overline{EO}_j > 0 \right] \end{array} \right\}$ then contact occurs
	then contact occurs, where point E is the point on the edge of cylinder <i>j</i> closest to the face of cylinder <i>i</i>	
Band–band: parallel axes	if $\left\{ \begin{array}{l} \left( \left  \mathbf{e}_{i,z}^G \cdot \mathbf{e}_{j,z}^G \right  = 1 \right) \text{ and} \\ \left[ \left  z_j^i \right  < \frac{1}{2} (L_i + L_j) \right] \text{ and} \\ \left[ (x_j^i)^2 + (y_j^i)^2 < (R_i + R_j)^2 \right] \end{array} \right\}$ , then contact occurs	
Band–band: skewed axes	if $\left\{ \begin{array}{l} \left[ d < R_i + R_j \right] \text{ and} \\ \left[ \left  l_i^* \right  < \frac{1}{2} L_i \right] \text{ and} \\ \left[ \left  l_j^* \right  < \frac{1}{2} L_j \right] \end{array} \right\}$ , then contact occurs	if $\left\{ \begin{array}{l} \left[ d < R_i + R_j \right] \text{ and} \\ \left[ \left  l_i^* \right  < \frac{1}{2} L_i \right] \text{ and} \\ \left[ \left  l_j^* \right  < \frac{1}{2} L_j \right] \text{ and} \\ \left[ R_i + R_j < \min \left( \frac{1}{2} L_i - \left  l_i^* \right , \frac{1}{2} L_j - \left  l_j^* \right  \right) \right] \end{array} \right\}$ , then contact occurs
	where <i>d</i> is the shortest distance between the axes of two cylinders. $l_i^*$ and $l_j^*$ are the shortest distance line between the cylinders intersecting the two cylinder axes at points defined by Vega and Lago [43]. $l_j^* = \frac{(\mathbf{e}_{i,z}^i \cdot \mathbf{e}_{j,z}^i)(\mathbf{e}_{i,z}^i \cdot \mathbf{x}_j^i) - (\mathbf{e}_{j,z}^i \cdot \mathbf{x}_j^i)}{1 - (\mathbf{e}_{i,z}^i \cdot \mathbf{e}_{j,z}^i)}$ , and $l_i^* = \mathbf{e}_{i,z}^i \cdot (\mathbf{x}_j^i + \mathbf{e}_{i,z}^i l_j^*)$ , where $\mathbf{e}_{i,z}^i = (0, 0, 1)^i$ and $\mathbf{e}_{j,z}^i = R^{ij}(0, 0, 1)^i$ , and $R^{ij}$ is the rotation matrix converting from cylinder <i>j</i> 's body fixed frame. $\mathbf{x}_j^i$ is cylinder <i>j</i> 's center position given in cylinder <i>i</i> 's body fixed frame of reference	
Band–edge	if $\left\{ \begin{array}{l} \left[ \left  z_E^i \right  < \frac{1}{2} L_i \right] \text{ and} \\ \left[ (x_E^i)^2 + (y_E^i)^2 < R_i^2 \right] \text{ and} \\ \left[ R_i - \sqrt{(x_E^i)^2 + (y_E^i)^2} < \left( \frac{1}{2} L_i - \left  z_E^i \right  \right) \right] \end{array} \right\}$ , then contact occurs	if not face–edge contact and $\left\{ \begin{array}{l} \left[ \left  z_E^i \right  < \frac{1}{2} L_i \right] \text{ and} \\ \left[ (x_E^i)^2 + (y_E^i)^2 < R_i^2 \right] \end{array} \right\}$ then contact occurs
	where point E is the point on the edge of cylinder <i>j</i> closest to the band of cylinder <i>i</i>	

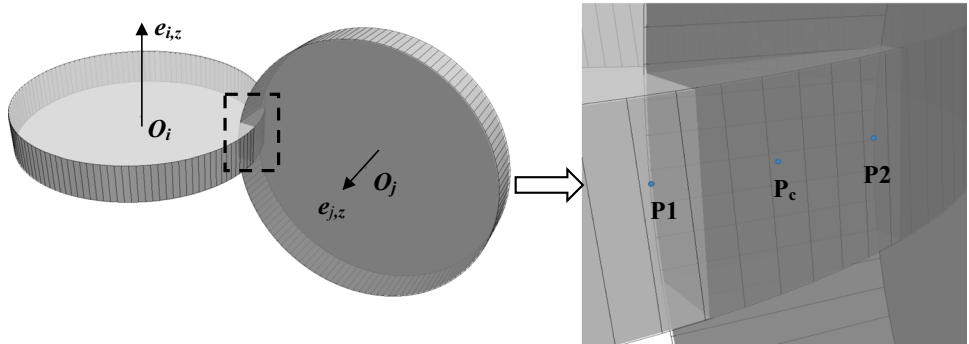
**Table 1** (continued)

Contact scenarios	Contact detection criteria proposed by Kodam et al. [1]	Contact detection criteria corrected by Guo et al. [2]
Edge-edge	$\text{if } \left\{ \begin{array}{l} \left[ \left  z_A^i \right  < \frac{1}{2} L_i \right] \text{ and} \\ \left[ \left( x_B^i \right)^2 + \left( y_B^i \right)^2 < R_i^2 \right] \end{array} \right\}$ <p>then contact occurs,                      where points <b>A</b> and <b>B</b> are the points on the edge of cylinder <i>j</i> and the band (point <b>A</b>) and face (point <b>B</b>) of cylinder <i>i</i> (see the Appendix for the calculation of these points)</p>	
Special contact	Not mentioned	if not face-edge contact $\text{and } \left\{ \begin{array}{l} \left[ \left  z_E^i \right  < \frac{1}{2} L_i \right] \text{ and} \\ \left[ \left( x_E^i \right)^2 + \left( y_E^i \right)^2 < R_i^2 \right] \text{ and} \\ \left[ \left  z_j^i \right  > \frac{1}{2} L_i \right] \text{ and} \\ \left[ \delta_a < \delta_r \right] \end{array} \right\}$ <p>then contact occurs</p>

**Fig. 2** Two special contact scenarios identified in this work



(a) Edge-edge contact



(b) Band-band (skewed) contact

particle and the axes are superimposed by the principal axes of inertia [44]. A vector can always be transformed from the space-fixed axes to the body-fixed axes, or vice versa via a transformation matrix which can be expressed by the quaternion method [45, 46]. More details about the transformation can be found elsewhere [47–49].

### 3 Simulation conditions

A simulation begins with the pouring of mono-sized and mono-shaped cylindrical particles into a rectangular box. Such a method has been commonly used elsewhere [13, 14]. A very small velocity with random direction, and a

random orientation of the cylinder principal axis  $OA$ , are assigned to each cylinder. These particles are then allowed to fall down under gravity with all above mentioned inter-particle forces effective. During this densification process, particles may collide with neighbouring particles and bounce back and forth. This dynamic process proceeds until all particles reach their stable positions with an essentially zero velocity as a result of the damping effect for energy dissipation, as done in the previous studies [13, 14].

Periodic boundary conditions are applied to the sidewalls to eliminate the wall effect. The bottom wall is assumed to have the same physical properties as particles. Packing density is calculated from the rectangular packing volume inside to eliminate the effects of the ragged or irregular top and the orientational ordered bottom for some aspect ratios. Graphics processing unit (GPU) which is capable to accelerate DEM simulations for non-spherical particles significantly [50] is employed in this work. For the packing cases of 10,000 cylinders in this work, a simulation can be completed within several minutes to hours, depending on the aspect ratio.

Cylinders are characterized by the band radius,  $R$  (or diameter  $D$ ), and the face-to-face length,  $L$ . Cylindrical particles with aspect ratios ( $L/D$ ) varying from 0.15 to 5.5 are used in this work to produce shapes from discs to rods. Particles with different aspect ratios have the same particle volume  $V_p$  (For  $L/D=1.0$ , the volume equivalent particle size  $d_p=L=D$  and  $V_p = \pi d_p^3/4$ , for  $L/D \neq 1.0$ ,  $d_p = \sqrt[3]{4V_p/\pi}$ ). The particle and bed properties used in the simulation cases are listed in Table 2.

## 4 Results and discussion

### 4.1 Packing pattern

Figure 3 shows the visual packing patterns of cylinders with different aspect ratios. As seen in Fig. 3a, particles with

**Table 2** Simulation settings for particles and bed

Parameters	Value
Volume equivalent particle size $d_p$ (mm)	10
Particle density $\rho_p$ (kg/m <sup>3</sup> )	2500
Particle shape (-)	Cylindrical
Particle aspect ratio $L/D$ (-)	0.15–5.5
Number of particles $N$ (-)	10,000
Bed size (Width×Thickness×Height) (mm)	200×200×2000
Young's modulus $E$ (N m <sup>2</sup> )	$1.0 \times 10^7$
Poisson's ratio $\nu$ , (-)	0.30
Sliding friction coefficient $\mu_s$ , (-)	0.3
Rolling friction coefficient $\mu_r$ , $d_p$	0.002
Normal damping coefficient $\mu_n$ , (-)	0.3
Tangential damping coefficient $\mu_t$ , (-)	0.3

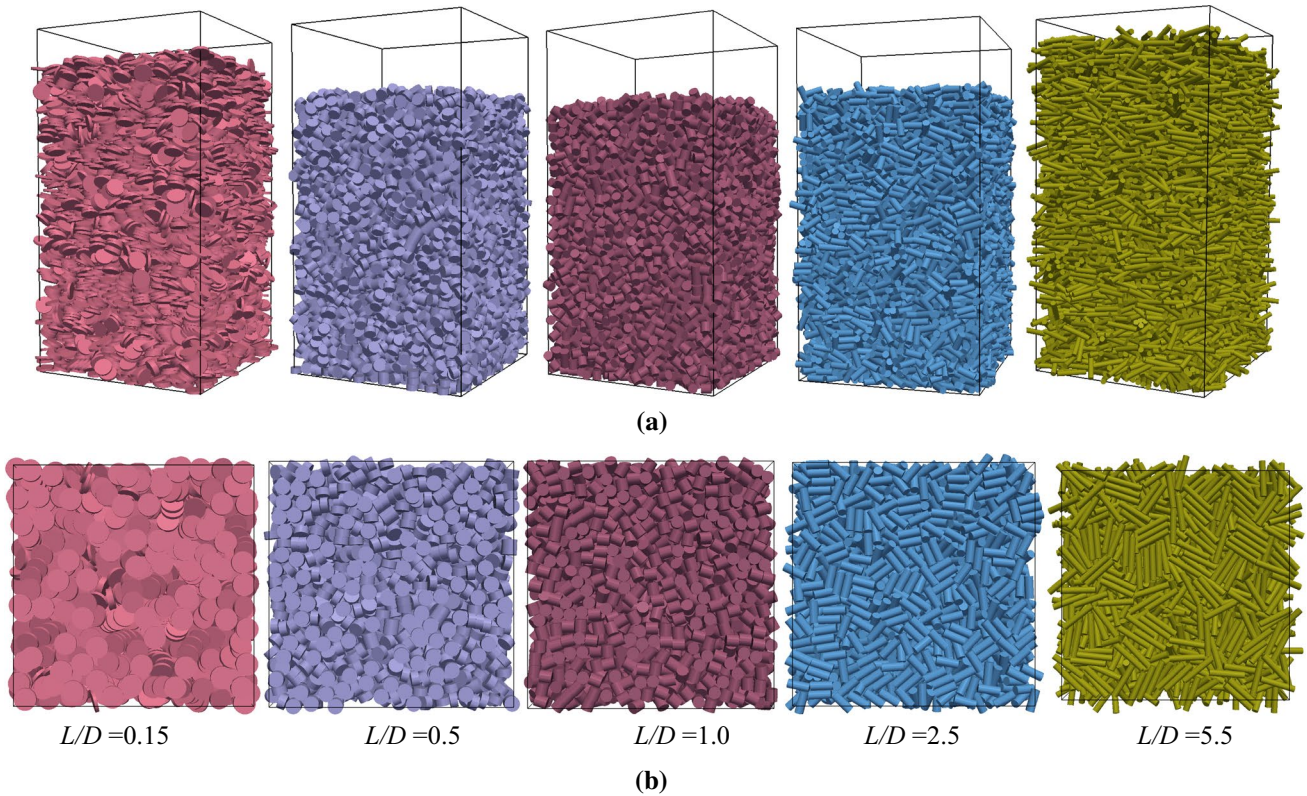
different aspect ratios shows different bed heights. When the aspect ratio is very small (e.g.  $L/D=0.15$ ) or large (e.g.  $L/D=5.5$ ), the bed height is higher than aspect ratio of 1.0, indicating a lower packing density for very platy and elongated particles. Moreover, the bed looks more ordered for platy and elongated particles, with the principal axis  $OA$  mainly pointing to the vertical direction for platy particles and horizontal direction for elongated particles. The figure also suggests that platy particles tend to form stacks of several particles in an approximately cylindrical shape, which is consistent with the literature [51, 52].

The ordered packing is even more obvious at the bed bottom. For example, when aspect ratio is 0.15, most of the particles contact with the bottom wall with their faces. When aspect ratio increases to 0.5, most of the particles still contact with the bottom wall with their faces, but a few contact with their bands. For aspect ratio of 1.0, particles with  $OA$  pointing to the vertical and horizontal directions are almost half to half. However, for elongated particles, most of the particles contact the bed bottom with the bands, that is,  $OA$  points to the horizontal direction. The ordered orientation in the whole bed and bed bottom for platy and elongated particles is reasonable according to the stable principle of minimum gravitational potential. To eliminate the wall effect and the top irregularity, in the quantitative analysis below, we will only consider particles in the centre with bed height from  $2d_p$  to  $H_{max} - 2d_p$ , where  $H_{max}$  is the maximum height (reduced by  $d_p$ ).

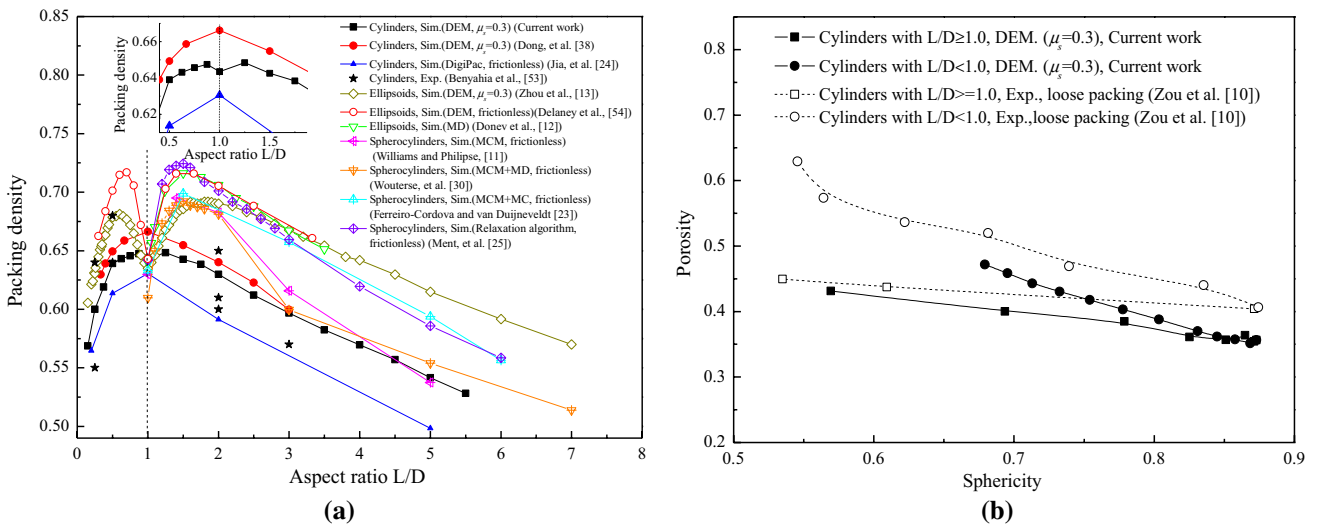
### 4.2 Packing density

Figure 4 quantitatively plots the variation of packing density or porosity with particle shape. As demonstrated in Fig. 4a, with aspect ratio increasing from 0.15, packing density increases to a maximum at around 0.875, then decreases a little at aspect ratio of 1.0 (see the insert in Fig. 4). After that, packing density increases again to reach another maximum at aspect ratio of around 1.25. However, when aspect ratio continues to increase, packing density decreases significantly. The simulation results are qualitatively comparable with the experimental results of Benyahia [53] and the simulation results of Jia et al. [24] using digital packing algorithm and Dong et al. [38] using orientation discretization database solution. However, Jia et al. [24] and Dong et al. [38] did not obtain the results for aspect ratio with a small deviation from 1.0, thus, there is not a cusp at aspect ratio around 1.0 in their work (see the insert in Fig. 4).

In this work, the DEM packing density results of cylinders are also compared with those of ellipsoids [12, 13, 54] and spherocylinders [11, 23, 25, 30] generated by different packed bed generation methods. For current DEM approach, the sliding friction coefficient  $\mu_s$  is set to 0.3 and the rolling friction coefficient  $\mu_r$  is set to 0.002, which were regarded



**Fig. 3** Packings of particles with different aspect ratios: **a** overall bed view and **b** bottom view



**Fig. 4** **a** variation of packing density with aspect ratio for cylinders simulated in this work and from [24, 38] and experimental results from [53], and in comparison with simulation results for ellipsoids [12, 13, 54] and spherocylinders [11, 23, 25, 30] (the insert: packing

densities for cylinders at aspect ratio around 1.0), **b** comparison of porosity–sphericity relationship with experimental results from Zou and Yu [10]

to have insignificant effect on packing density of spheres [55]. For spherocylinders,  $L$  is the length of the particle, rather than only the cylinder part. It can be seen that similar

tendency for the two peaks and a cusp at aspect ratio around 1.0 are also found for ellipsoids [12, 13, 54] and spherocylinders [11, 23, 30]. However, there is only a small cusp (in



this work) or even no cusp (by Jia et al. [24] and Dong et al. [38]) at aspect ratio of 1.0 for cylinders (see the insert in Fig. 4). This is reasonable because ellipsoids and spherocylinders become spheres at aspect ratio of 1.0 (singular shape change), while particles are still cylindrical at aspect ratio of 1.0 for cylinders. Therefore, a small deviation from aspect ratio of 1.0 brings less change in the particle shape for cylinders, thus less variation in packing density. Moreover, for elongated particles with aspect ratio larger than 2.0, the order of packing density of frictionless packings (upper bound of packing density) for the three particle shapes is: cylinders < spherocylinders < ellipsoids.

Figure 4b also plots the variation of porosity with particle sphericity (defined as the ratio of the surface area of a sphere which has the same volume as a given particle to the surface area of the particle). It shows that with the decrease of particle sphericity, porosity increases for both the cases of  $L/D \leq 1.0$  and  $L/D \geq 1.0$ . However, for the same sphericity, platy particles with  $L/D \leq 1.0$  have a higher porosity than elongated particles. The simulation results are generally consistent with the experimental results [10]. The difference might be resulting from the difference in packing method or the particle properties. Poured packing was used to generate a loose random packing in current DEM simulation. In the experiment [10], the cylinder was tipped horizontally and slowly rotated about its axis and gradually returned to the vertical position to produce a loose random packing which may cause more particle interlocks. Moreover, glass cylinders are used in the DEM simulation, and wooded rods are used in the experiments. A smaller particle density could also lead to a looser bed with higher porosity.

It is known that for sufficient high aspect ratios, packing density is inversely proportional to the excluded volume for spherocylinders [11, 52]. Thus, it is necessary to study the effect of aspect ratio on excluded volume for non-spherical particles. Here the excluded volume of a particle refers to the volume that is inaccessible to other particles in the system as a result of the presence of the reference particle. For platy cylinders, when  $L/D$  reduces, the increasing effect of planar face induces considerable alignment and ordering of particles, which can reduce the excluded volume effect. Therefore, we only study the excluded volume effect of elongated cylinders in the present work. We also compare the excluded volume effect of cylinders with another two typical elongated particles: spherocylinders and ellipsoids.

The expression of excluded volume for three types of elongated particles can be obtained in the literature. For two ellipsoids, the excluded volume can be expressed according to Eq. (6a), where  $V_i$  and  $V_j$  are the particle volume,  $A_i$  and  $A_j$  are the particle surface area, and  $R_i$  and  $R_j$  are the mean radii of curvature at the closest point between two particles [56]. According to Onsager [57], the excluded volume for a pair of cylinders of lengths  $L_i$  and  $L_j$ , diameter  $D$  and

relative orientation  $\gamma$  is given by Eq. (6b), where  $E(\sin(\gamma))$  denotes the elliptic integral of the second kind, given as  $E(\sin(\gamma)) = \int_0^{\pi/2} (1 - \sin^2(\gamma) \sin^2(\phi)) d\phi$ . For two spherocylinders the excluded volume is expressed according to Eq. (6c), where  $\gamma$  is also the angle between the long axes of the two spherocylinders [58, 59].

$$V_{ex,ij,ellipsoid} = V_i + V_j + (A_i R_j + A_j R_i) \quad (6a)$$

$$V_{ex,ij,cylinder} = \frac{\pi}{4}(L_i + L_j)D^2 + \frac{\pi}{2}D^3 \sin(\gamma) + 2L_i L_j D \sin(\gamma) + \frac{\pi}{4}(L_i + L_j)D^2 |\cos(\gamma)| + (L_i + L_j)D^2 E(\sin(\gamma)) \quad (6b)$$

$$V_{ex,ij,spherocylinder} = (D_i + D_j)L_i L_j |\sin(\gamma)| + \frac{\pi}{4}(D_i + D_j)^2(L_i + L_j) + \frac{\pi}{6}(D_i + D_j)^3 \quad (6c)$$

From above equations, the excluded volume depends on the particle orientation. For an aspect ratio of the order unity, the maximum excluded volume is found between the parallel and perpendicular orientation ( $\gamma = 90^\circ$ ) [51]. Thus, the expression of the orientational averaged excluded volume is needed. To compare the orientational averaged excluded volume  $V_{ex}$  for cylinders, ellipsoids and spherocylinders, particles with the same volume  $V_p$  are used and  $V_{ex}$  is normalized by  $V_p$ .

The orientational averaged excluded volume for equal spheroids [52] with volume  $V_{p,spheroid}$  is

$$\left(\frac{V_{ex}}{V_p}\right)_{spheroid} = 2 + \frac{3}{2}z \left[ 1 + \frac{(1 - \varepsilon^2)}{2\varepsilon} \ln\left(\frac{1 + \varepsilon}{1 - \varepsilon}\right) \right] \left[ \sqrt{1 - \varepsilon^2} + \frac{\arcsin(\varepsilon)}{\varepsilon} \right] \quad (7a)$$

where  $z = L/D$  for prolate spheroids and  $D/L$  for oblate spheroids and  $\varepsilon^2 = 1 - 1/z^2$ . Therefore, for prolate ellipsoid in the limit of long rods ( $L/D \gg 1$ ),  $\varepsilon^2 = 1$ , and the  $(V_{ex}/V_p)_{ellipsoid}$ —aspect ratio curve is almost linear with a slope of  $(3\pi/4)L/D$ .

Onsager [57] calculated the ratio of excluded volume to particle volume between two cylinders, the averaged  $(V_{ex}/V_p)_{cylinder}$  over an isotropic orientational distribution of cylinders is  $V_{ex,cylinder} = (\pi D/2)[L^2 + (\pi + 3/2)LD + \pi D^2/4]$ , and

$$\left(\frac{V_{ex}}{V_p}\right)_{cylinder} = 2\pi + 3 + 2\frac{L}{D} + \frac{\pi}{2}\frac{D}{L} \quad (7b)$$

Therefore, for cylinders in the limit of long rods ( $L/D \gg 1$ ), the  $(V_{ex}/V_p)_{cylinder}$ —aspect ratio curve is almost linear with a slope of  $2L/D$ .

Similarly, the orientation average exclude volume of a pair of random spherocylinders [60]:  $V_{ex,spherocylinder} = (\pi/2)$

$L^2D + 2\pi D^2L + (4/3)\pi D^3$ , and  $V_p = (\pi/6)D^3 + (\pi/4)D^2L$ , and therefore

$$\left(\frac{V_{ex}}{V_p}\right)_{\text{spherocylinder}} = \left[6\left(\frac{L}{D}\right)^2 + 24\frac{L}{D} + 16\right] / \left(2 + 3\frac{L}{D}\right) \tag{7c}$$

Therefore, for spherocylinders in the limit of long rods ( $L/D \gg 1$ ), the  $(V_{ex}/V_p)_{\text{spherocylinder}}$  - aspect ratio curve is almost linear with a slope of  $2L/D$  as well.

The variation of orientational averaged excluded volume  $V_{ex}/V_p$  with aspect ratio  $L/D$  according to Eqs. (7a)–(7c) is plotted in Fig. 5. It can be seen that at low aspect ratio, the relationship between  $V_{ex}/V_p$  and aspect ratio  $L/D$  slightly deviates from linear. However, at higher aspect ratio,  $V_{ex}/V_p$  generally increases linearly with aspect ratio  $L/D$ , consistent with the above theoretical analysis. Cylinders and spherocylinders have the same slopes, but ellipsoids have a slightly larger slope than the other two types. Note that in this figure, the particle volume  $V_p$  is kept the same for different aspect ratios and particle shapes, therefore even at high  $L/D$ , the three particle shapes have different  $V_{ex}$ . When the aspect ratio is smaller than 11.5, the order of  $V_{ex}$  for different particle types are: cylinders > spherocylinders > ellipsoids, which is corresponding to the order of packing density as shown in Fig. 4: cylinders < spherocylinders < ellipsoids. It should be noted that when aspect ratio is close to 1.0, spherocylinders and ellipsoids are close to spheres, and the packing is an outcome of a competition between local caging effect and excluded volume effect [11, 14]. Moreover, at a high aspect ratio, e.g.,  $L/D > 11.5$ ,  $V_{ex}$  of ellipsoids gradually exceeds that of spherocylinders and approaches that of cylinders as ellipsoids have a larger slope than cylinders and spherocylinders.

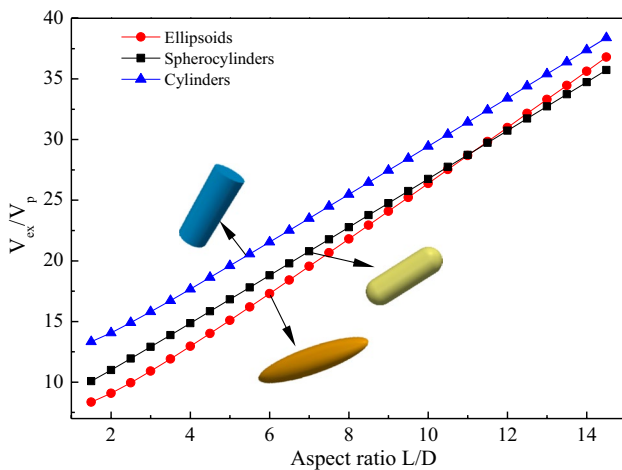


Fig. 5 Variation of orientational averaged excluded volume with aspect ratio  $L/D$  for particle pairs with different shapes

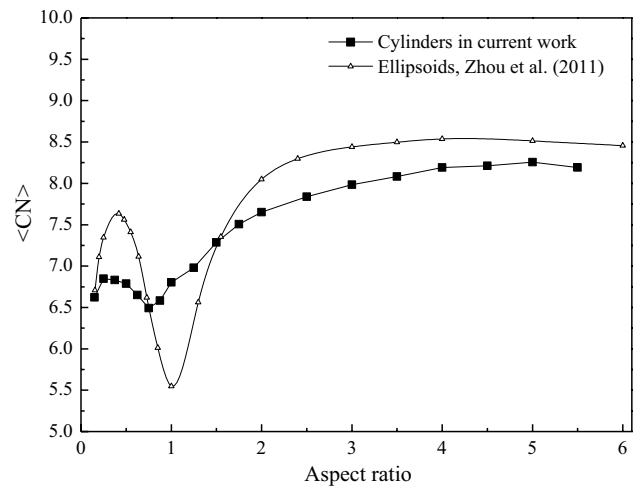


Fig. 6 Ensemble-averaged coordination number  $\langle CN \rangle$  for cylinders in the current work and for ellipsoids of Zhou et al. [13] for different aspect ratios

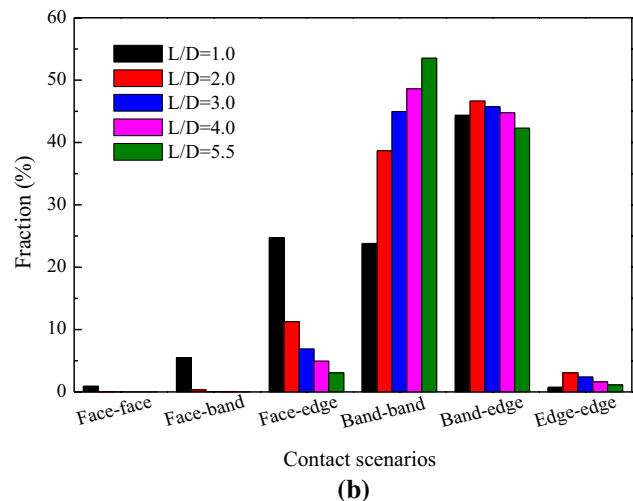
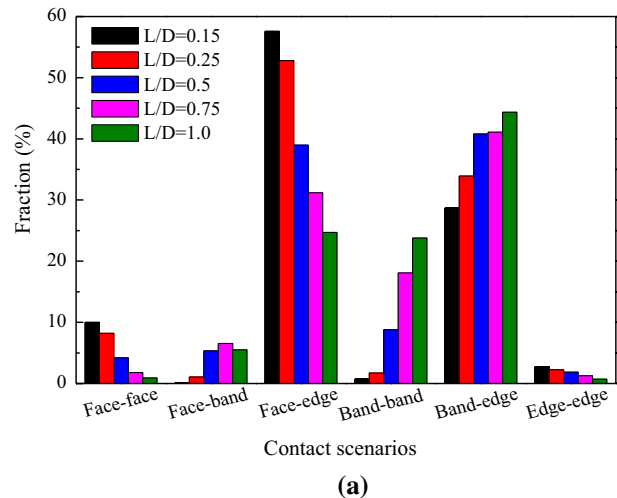
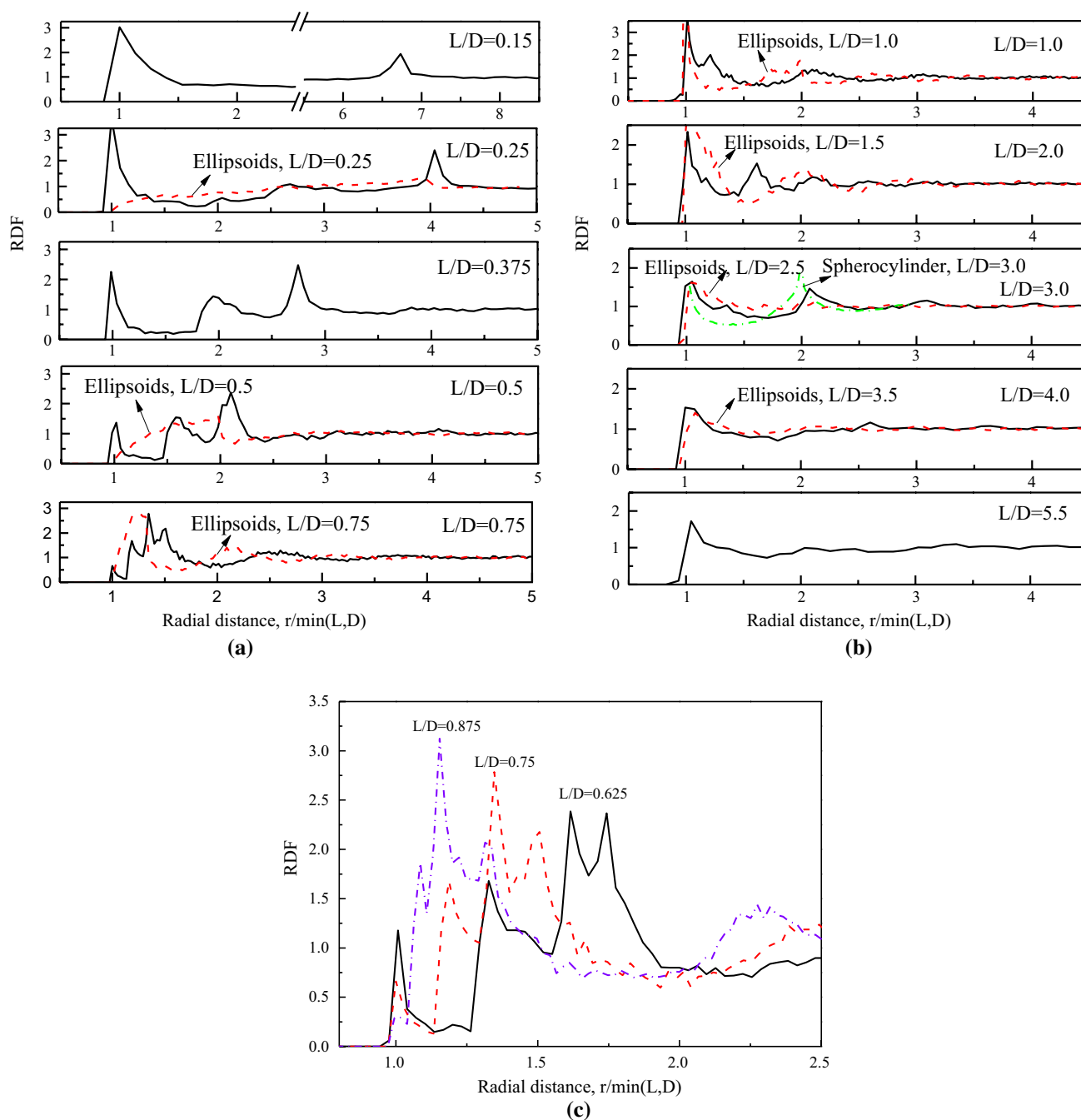


Fig. 7 Distribution of contact scenarios for cylinders with different aspect ratios: a  $L/D \leq 1.0$  and b  $L/D \geq 1.0$



**Fig. 8** Radial distribution functions for the packing of cylinders with different aspect ratios. **a**  $L/D \leq 1.0$ ; **b**  $L/D \geq 1.0$  (data of dash curves from [14] and data of dash dot curve from [11]); and **c** local RDF for  $L/D$  between 0.625 and 0.875

### 4.3 Particle contacts

Coordination number (CN) reflects the number of contacting neighbours per particle, which is usually used to characterise packing structures. CN is here representing a real contact between particles, and has different contact types as shown in Figs. 1 and 2. For simplicity, we only consider their averages, rather than their distributions. The ensemble-averaged

$\langle CN \rangle$  is plotted with aspect ratio in Fig. 6. When aspect ratio increases from 0.15,  $\langle CN \rangle$  first increases slightly and then decreases obviously. The lowest  $\langle CN \rangle$  is reported at aspect ratio of around 0.75. When the aspect ratio further increases,  $\langle CN \rangle$  increases dramatically and asymptotes towards 8.2 which is smaller than the value of MCM-MD contact number (9.8) and upper limit (10) for uncompacted rods [22].

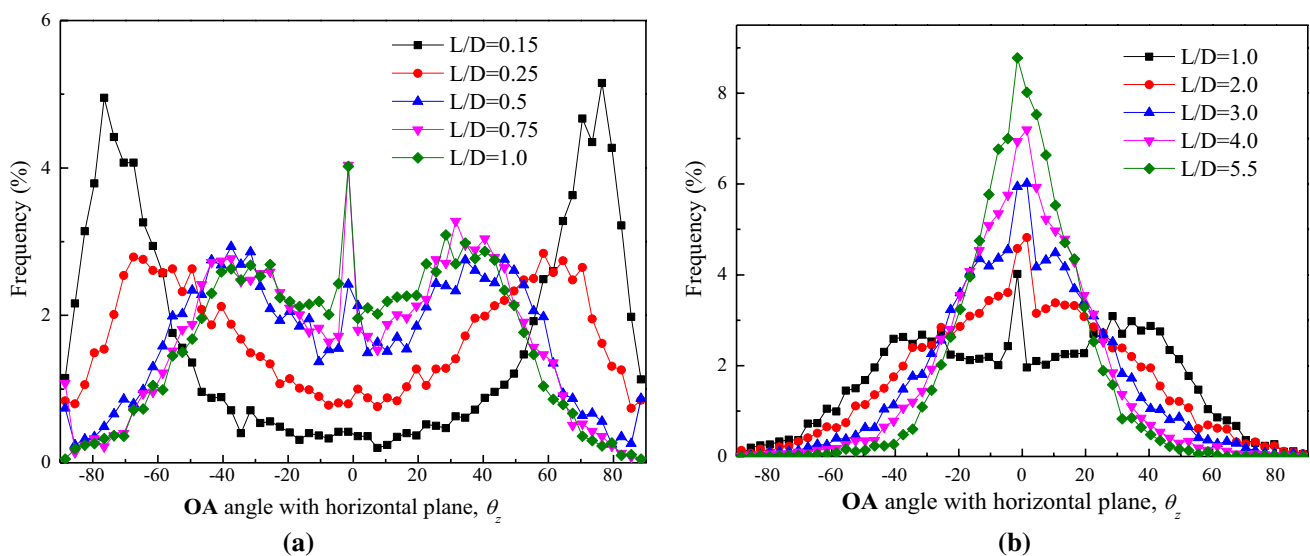


**Fig. 9** Variation of OA angle with the horizontal plane for cylinders with different aspect ratios

$\langle \text{CN} \rangle$  for cylinders and ellipsoids are also compared in this figure. Comparing with ellipsoids [13], the growth of  $\langle \text{CN} \rangle$  with aspect ratio is much slower for elongated cylinders, which is generally consistent with Blouwolf and Fraden [61]. Moreover, the general variation tendencies of ellipsoids and cylinders are consistent, but ellipsoids have a larger difference in  $\langle \text{CN} \rangle$  with aspect ratio. Specifically, for platy particles, when aspect ratio decreases from 0.75, they have much smaller  $\langle \text{CN} \rangle$  than ellipsoids. The largest difference appears at aspect ratio of around 0.375. The possible reason for this is that platy cylinders tend to form stacks of several particles, which reduces the chance for others particles to contact with both faces of a cylinder. The difference in  $\langle \text{CN} \rangle$  becomes small when aspect ratio reduces to 0.15 where cylinders and oblate ellipsoids are close in shape. When aspect ratio is near 1.0, cylinders have a much higher  $\langle \text{CN} \rangle$  than ellipsoids. From the aspect of constraint counting, this is reasonable because an ellipsoid become a sphere at aspect ratio of 1.0, which needs  $d+1 \sim 2d$  (for frictional spheres) to cage it [62]. When the aspect ratio slightly deviates from 1.0, it become non-spherical, which requires more contact points due to the additional orientational degrees of freedom [63]. For cylinders, a small deviation of aspect ratio from 1.0 does not change the degrees of freedom and the number of constraints. When aspect ratio is larger than 1.5, ellipsoids have a higher  $\langle \text{CN} \rangle$  than cylinders as a result of the lower excluded volume as discussed in Sect. 4.2.

As shown in Figs. 1 and 2, there are generally six different contact scenarios for cylinders: face–face, face–band, face–edge, band–band (parallel and skewed), band–edge, and edge–edge. The distribution of different contact scenarios can be significantly affected by particle aspect ratio,

as shown in Fig. 7. For platy cylinders, as shown in Fig. 7a, the dominant contact scenario is the face–edge contacts, followed by the band–edge contacts. There are also considerable part of face–face contacts and small amount of face–band, band–band and edge–edge contacts. When aspect ratio increases, the fraction of face–edge contacts significantly reduces, and the dominant contact scenario is the band–edge contacts. In the meantime, the fraction of band–band contacts also grows obviously, while the fraction of ordered packing structure, the face–face contacts, reduces. There is only a slight decrease in the edge–edge contacts.

For elongated cylinders, as illustrated in Fig. 7b, the major contact scenarios are the band–edge and band–band contacts, and there are also considerable amount of face–edge contacts. With aspect ratio increases from 1.0, the fraction of band–band contacts increases significantly, while the fraction of face–edge contacts drops markedly. There is only a small change in the fraction of band–band contacts. Compared with platy cylinders, elongated cylinders have very limited face–edge, face–face and face–band contacts.

#### 4.4 Radial distribution functions (RDF)

RDF is commonly used to describe the particle contact condition and positional order of a packing. It is defined as the probability of finding one particle centre at a given distance from the centre of a given particle. For spheres, it is given by  $g(r) = N(r)/4\pi r^2 \Delta r \rho_0$ , where  $N(r)$  is the number of particles centres situated at a distance between  $r$  and  $r + \Delta r$  of a given particle, and  $\rho_0$  is the number of particles per unit volume in the packing, given by  $\rho_0 = 6\varepsilon_s/(\pi d_p^3)$ , where  $\varepsilon_s$  is the packing density. The similar conception is extended to

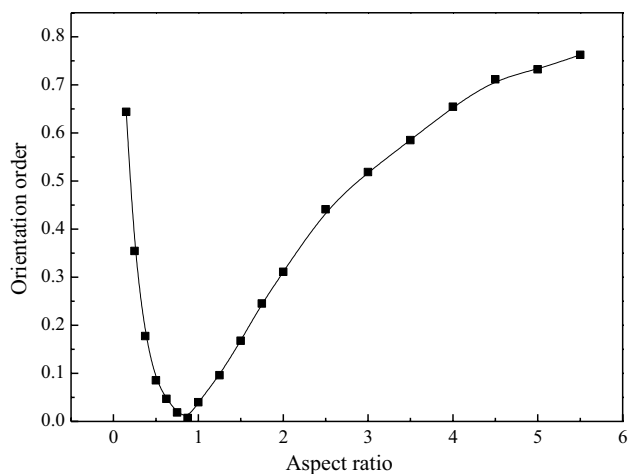


Fig. 10 Variation of orientation order with aspect ratio

cylindrical particles. Different choices of  $\Delta r$  lead to almost indistinguishable results [64]. In the present calculation,  $\Delta r = 0.02d_p$  and the so-called radial distance is made with the reference to the minimum of particle face diameter  $D$  and axis length  $L$ .

Figure 8 shows the RDF of cylinders with different aspect ratios. When aspect ratio is small, e.g.,  $L/D = 0.15$  and  $0.25$ , only two peaks at the radial distance near  $L$  and  $D$  (e.g. 1.0 and 6.67 for aspect ratio of 0.15) are observed, and the peak density at the radial distance near  $L$  is higher than that near  $D$ . These two peaks are corresponding to three major contact types: face-face/face-edge and band-edge. When aspect

ratio is between 0.375 and 1.0, three peaks are observed at radial distance near  $L$ ,  $(L+D)/2$ , and  $D$ , corresponding to the face-edge, band-band and band-edge contacts.

For aspect ratio between 0.625 and 0.875, as shown in Fig. 8c, the third peak divides into two small peaks, indicating more diverse contact modes for these aspect ratios. For example, the first peak in the divided two peaks is close to the radial distance  $D$  (e.g., the radial distance =  $1.625L = 1.01D$  for  $L/D = 0.625$ ). The second peak is at radial distance around  $0.5L + 0.75D$ , and there could be several kinds of contact types leading to this peak. With the increase of aspect ratio, all these peaks move towards 1.0. When aspect ratio is 1.0, these three peaks overlap at the radial distance of 1.0.

When aspect ratio is 1.0, there are also peaks at the radial distance around  $\sqrt{5}/2$  and 2.0, as shown in Fig. 8b. This is similar to the concept of edge-sharing in-plane equilateral triangles and three particles along a line for spheres [14]. However, the RDF of cylinders is much lower than that of spheres. That is, the long-range position order of cylinders is worse than spheres. When aspect ratio is larger than 3.0, the second and third peaks at the radial distance of  $(L+D)/2$  and  $L$  become less obvious and even disappear, which means that there are less face-face and face-band contacts, and the band-band contacts dominate in the packing of elongated cylinders.

The RDF of cylinders can be compared with that of ellipsoids and spherocylinders from the literature [11, 14], as plotted in Fig. 8. It can be seen that for platy cylinders, the RDF shows quite different intensity at the same radial

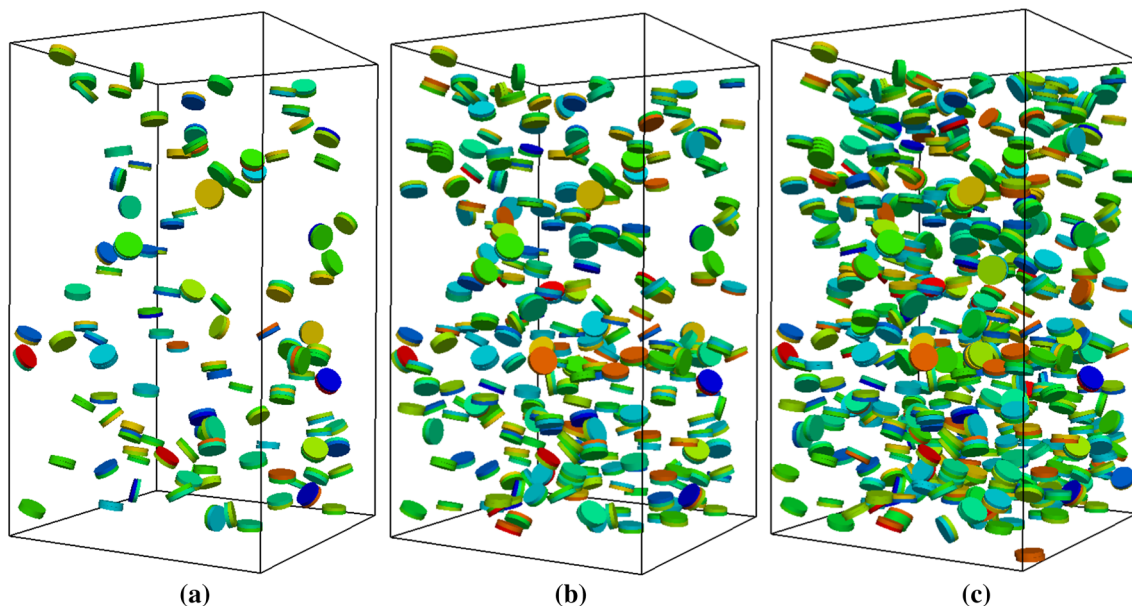
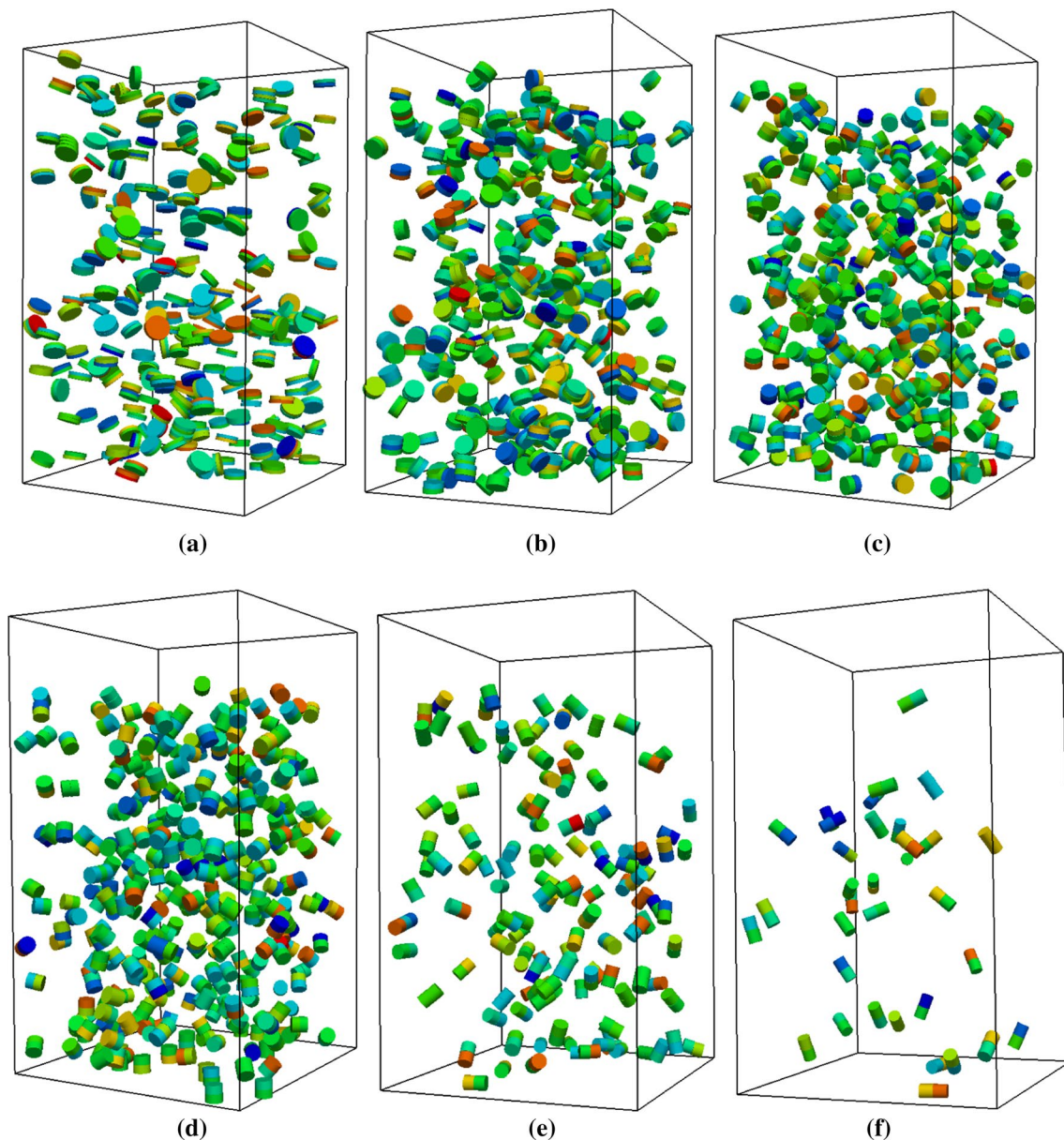


Fig. 11 Effect of the difference in the critical radial distance  $\delta_{cr}$  between two contact particles in the stacks for cylinders with aspect ratio of 0.15: **a**  $\delta_{cr} \leq 0.05R$ , **b**  $\delta_{cr} \leq 0.1R$  and **c**  $\delta_{cr} \leq 0.15R$

distance. For oblate particles, the first peak at around radial distance of 1.0 is very wide, and even becomes obscure when aspect ratio reduces. However, for elongated particles, cylinders, spherocylinders and ellipsoids show some similar peaks, especially at high aspect ratios. For example, they all show a peak at radial distance around 1.0. This implies that elongated cylinders, spherocylinders and prolate particles are similar in packing structure, but the existence of the planar faces of a platy cylinder makes the packing structure of disks quite different from that of smooth curved oblates.

#### 4.5 Orientation analysis

Orientation is one of the most important features of non-spherical particles differing from spheres. As has been illustrated in the packing pattern shown in Fig. 3, particle orientation varies with particle shape significantly. Figure 9 show the variation of **OA** angle with the horizontal plane ( $\theta_z$ ) for different aspect ratios. For platy cylinders with aspect ratio of 0.15, the highest frequency of  $\theta_z$  is observed at around  $-75^\circ$  and  $75^\circ$ , indicating that most platy cylinders have **OA** pointing to and almost paralleling to the vertical direction, consistent with Fig. 3. With the increase of aspect ratio, the



**Fig. 12** Stacks in the packing of platy cylinders of different aspect ratios at  $\delta_{cr} \leq 0.1R$ : **a**  $L/D=0.15$ , **b**  $L/D=0.25$ , **c**  $L/D=0.375$ , **d**  $L/D=0.5$ , **e**  $L/D=0.75$  and **f**  $L/D=1.0$  (particles are coloured according to their particle orientation vector)

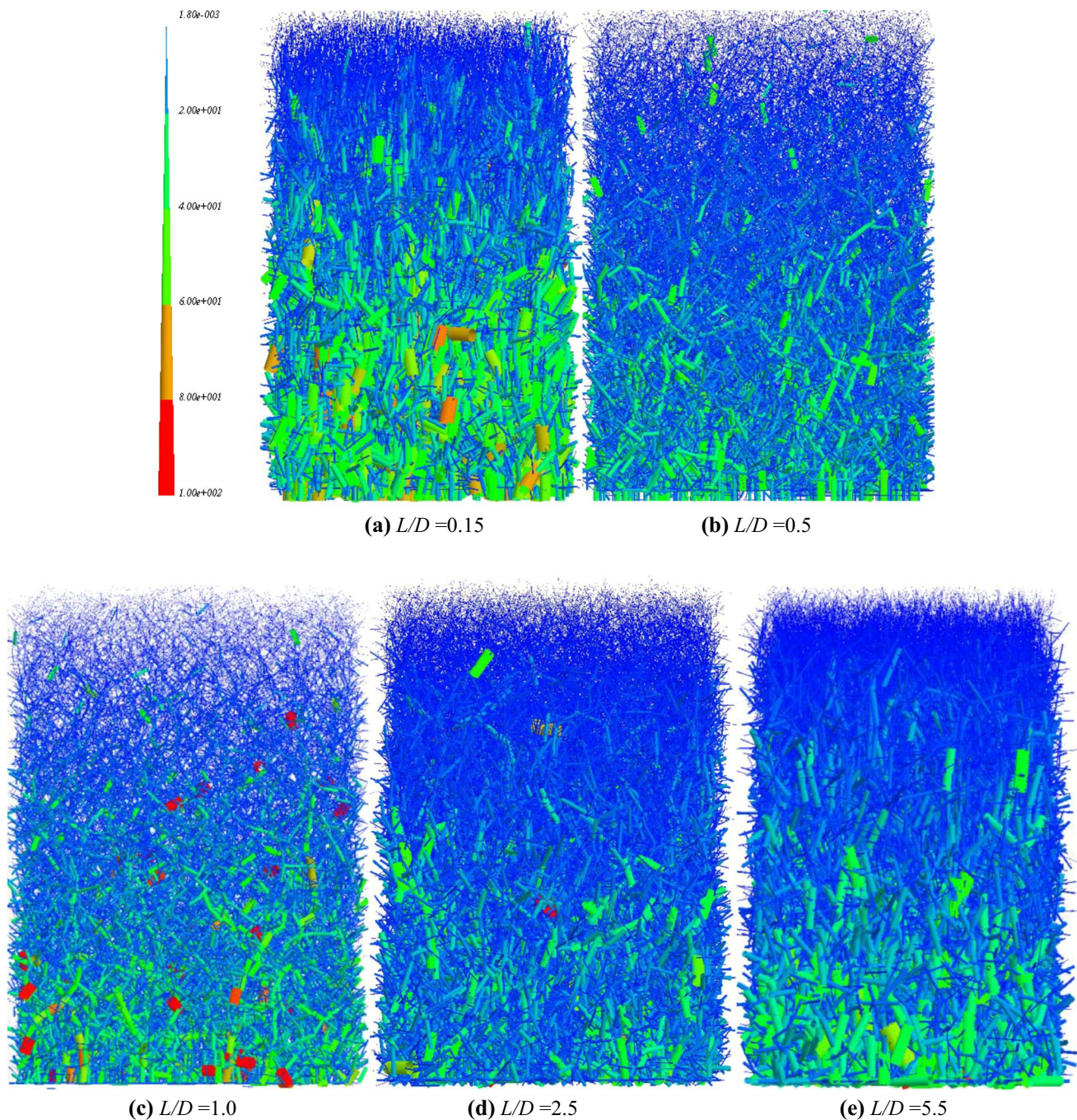


**Fig. 13** Contact force network in the packing of cylinders with different aspect ratios, coloured by the magnitude of total contact force  $\|\mathbf{f}_{ij}\|/m\mathbf{g}$ , the line thickness is proportional to force magnitude. **a**  $L/D=0.15$ , **b**  $L/D=0.5$ , **c**  $L/D=1.0$ , **d**  $L/D=2.5$ , **e**  $L/D=5.5$

$\theta_z$  peaks move towards zero, and the frequency at the peaks reduces significantly. That means that particle orientation becomes more random in the bed. When aspect ratio is close to 0.5, there is a small peak at  $\theta_z$  of zero. This implies that a considerable number of particles have **OA** pointing to the horizontal plane. For elongated cylinders, with the increase of aspect ratio, the frequency of the peak at  $\theta_z=0$  increases obviously, and becomes the dominant peak. Therefore, **OA**

of elongated cylinders tend to point to the horizontal plane, which is also consistent with Fig. 3.

To be quantitative, the spatial degree of orientational alignment of non-spherical particles is characterized using a scalar order parameter called an orientational order  $\chi_\theta$  [16, 65]. For prolate particles, the orientational order is defined as  $\chi_\theta = 1.5 \left\{ \left( \sum_{i=1}^N \cos 2(\theta_i - \pi/2) \right) / N - 1/3 \right\}$ . For oblate

particles the order parameter is given by  $\chi_\theta = 0.75 \left\{ \left( \sum_{i=1}^N \cos(2\theta_i) \right) / N + 1/3 \right\}$ , where  $\theta$  is the angle between the largest semi-axis of spheroids and the vertical axis, and the average is taken over all the particles in the sample. The orientational order  $\chi_\theta$  becomes zero when particles are all randomly oriented, and one when particles are all ordered, oriented in a plane. The effect of particle shape on bulk-averaged orientation order is shown in Fig. 10. It can be seen that the orientation order curve shows a cusp at aspect ratio of 0.875. When the aspect ratio deviates from 0.875, the orientation order increases dramatically, indicating more ordered packing structure. For aspect ratio of 5.5, the orientation order reaches as high as 0.76, implying most particles have **OA** pointing to the horizontal plane, which is consistent with Fig. 9.

As shown in Fig. 3, platy particles tend to form stacks of several particles. Note here a particle  $i$  is identified to belong to a stack when its axial distance to the neighbouring particle  $j$  is smaller than  $0.5 \cdot (L_i + L_j)$  and the radial distance is smaller than a critical value  $\delta_{cr}$ . In order to study the tendency of forming stacks for different aspect ratios and how many particles are contained in a stack, the stacks in a packing are showed in Fig. 11. It can be seen that the total number of stacks in the packings significantly increases with the difference in the critical radial distance  $\delta_{cr}$ . For most of the stacks, there are only 2 disks. However, there are also stacks composed of 3 or 4 disks. The total numbers of stacks in the packing differ obviously for different aspect ratios, as shown in Fig. 12. With the increases of aspect ratio, the number of stacks increases somewhat and then decreases dramatically when aspect ratio increases to 1.0. For aspect ratios between 0.15 and 0.625, most stacks contain 2 particles and a few contain 3 or 4 particles, but for aspect ratios of 0.75 and 1.0, all the stacks are found to contain only 2 particles. This is consistent with Alan et al. [52] who found that the number of particles per column/stack in the packing of cut spheres increases when the particles are more platy.

#### 4.6 Force network

The force network is also analysed and plotted in Fig. 13. Here, the forces between particles or between a particle and base wall are demonstrated by the thickness of sticks that are proportional to the magnitude of the normal contact force. Each stick represents a contact between two particles, and its direction represents the direction of the normal contact force. As seen in Fig. 13, obvious force gradient in the vertical direction can be observed. That is, most forces are in the vertical direction. For  $L/D=0.15$ , some large forces can be observed in the vertical direction due to the stacking of particles, which have the origin from the bed bottom. With the increase of  $L/D$  from 0.15 to 1.0, the particle stacking phenomenon becomes less obvious, the number of large forces become less, and the

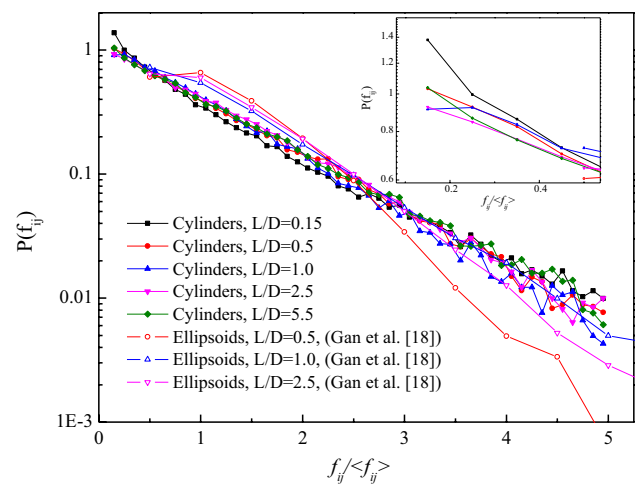


**Fig. 14** Probability distribution of total contact force for different particle shapes

force magnitude becomes more uniform within a bed. For  $L/D=1.0$ , the force directions are diverse. This is because that the contact force does not necessarily pass through a particle centre, thus the long force chains, which are normally observed in the packing of coarse spheres [18], cannot be formed. From  $L/D=1.0$  to 5.5, an increase in the force gradient can be seen. Moreover, there are more small forces in the horizontal direction, corresponding to the increase in the band-band contact as shown in Fig. 7b.

One way to quantify the force variation in disordered materials is to measure the probability distribution of forces  $P(f_{ij})$  in the grain assembly. Figure 14 shows the probability distribution of forces of total contact force for the aspect ratios mentioned in Fig. 13. It can be seen that for cylinders with different aspect ratios, the probability distributions of forces  $P(f_{ij})$  are quite close, except that both flat and elongated cylinders have more small (e.g.,  $f_{ij}/\langle f_{ij} \rangle < 0.2$ ) and also more large (e.g.,  $f_{ij}/\langle f_{ij} \rangle > 4.0$ ) forces. This is consistent with the force networks as shown in Fig. 13 and also consistent with the Qian et al. [66] in random close packings of cylinders. However, this is quite different from ellipsoidal particles [18] which show large difference in  $P(f_{ij})$  for different aspect ratios. This is again caused by the geometry changes from spheres to ellipsoids when aspect ratio slightly deviates from 1.0.

## 5 Conclusions

DEM has been used to study the packing structure in packed bed of cylindrical particles. Two special contact scenarios are found not able to be detected according to the detection criteria proposed by Kodam et al. [1] and Guo et al. [2]. New



contact detection methods are proposed for these contact scenarios. Based on this, this work focuses on studying the effect of aspect ratio on packing structure at both macroscopic and microscopic levels. The results are summarized below:

1. The packing density-aspect ratio curves show two small peaks at aspect ratio of 0.625 and 1.25, and a small cusp at aspect ratio of 1.0. When aspect ratio is larger than 2.5, the order of excluded volume for different particle types are: cylinders > spherocylinders > ellipsoids, which is corresponding to the order of packing density: cylinders < spherocylinders < ellipsoids.
2. The lowest mean coordination number  $\langle \text{CN} \rangle$  is reported at aspect ratio around 0.75. When aspect ratio is larger than 1.5, cylinders have a lower  $\langle \text{CN} \rangle$  than ellipsoids, due to higher excluded volume. For platy cylinders, the dominant contact scenario is the face-edge contacts, followed by the band-edge contacts. For elongated cylinders, the major contact scenarios are the band-edge and band-band contacts.
3. When aspect ratio is small (0.15 or 0.25), only two peaks in RDF are observed when the critical radial distances are near  $L$  and  $D$ . When aspect ratio is between 0.375 and 3.0, three peaks are observed at the radial distance near  $L$ ,  $(L+D)/2$  and  $D$ . With the increase of aspect ratio, all these peaks move towards to 1.0; and for aspect ratio of 1.0, these three peaks overlap at the radial distance of 1.0. When aspect ratio is larger than 3.0, the second and third peaks at the radial distance of  $(L+D)/2$  and  $L$  become less obvious and even disappear. Elongated cylinders, spherocylinders and prolate particles are similar in RDF, but the existence of the planar faces of a platy cylinder makes the RDF (and thus packing structure) of disks quite different from that of smooth-curved oblates.
4. Most platy cylinders have their orientation  $\mathbf{OA}$  pointing to and almost paralleling to the vertical direction, while the  $\mathbf{OA}$  of elongated cylinders tend to point to the horizontal plane. Platy particles tend to form stacks composed of 2-4 particles for different aspect ratios. With aspect ratio approaches 1.0, the number of stacks reduces obviously.
5. Unlike coarse spheres, long force chains cannot be formed for cylinders with  $L/D=1.0$ . The force gradient increases and force magnitude becomes less uniform when  $L/D$  deviates from 1.0. For cylinders with different aspect ratios, the total contact force distributions are quite close, except that flat and elongated cylinders have more small and large forces.

**Acknowledgements** The authors are grateful to the Australian Research Council (ARC IH140100035) for the financial support of

this work, and the NCI National Facility and Monash Massive for the support of computation.

## Compliance with ethical standards

**Conflict of interest** The authors declare that they have no conflict of interest.

## Appendix

Any point  $\mathbf{P}$  on the edge circle of cylinder  $j$  can be specified in cylinder  $i$ 's frame of reference as [1, 67]:

$$\mathbf{P}(\theta) = \mathbf{C}_j^i + R_j \cos(\theta) \mathbf{u} + R_j \sin(\theta) \mathbf{v} \quad (\text{A1})$$

where  $\mathbf{C}_j^i$  is the centre of cylinder  $j$ 's edge circle.  $\mathbf{u}$  and  $\mathbf{v}$  are the two perpendicular unit vectors in the plane containing the edge circle of  $j$ . These vectors are defined as follows:

$$\mathbf{u} = \frac{\mathbf{e}_{j,z}^i \times (0, 0, 1)^i}{\left| \mathbf{e}_{j,z}^i \times (0, 0, 1)^i \right|} \quad (\text{A2})$$

and

$$\mathbf{v} = \frac{\mathbf{u} \times \mathbf{e}_{j,z}^i}{\left| \mathbf{u} \times \mathbf{e}_{j,z}^i \right|} \quad (\text{A3})$$

Point  $\mathbf{A}$  (or  $\mathbf{A1}$  and  $\mathbf{A2}$  in Fig. 2a) is obtained by equating the radial component of point  $\mathbf{P}$  to the radius of cylinder  $j$ , and then solving for  $\theta$ :

$$P_x^2 + P_y^2 = R^2 \quad (\text{A4})$$

And point  $\mathbf{B}$  (or  $\mathbf{B1}$  and  $\mathbf{B2}$  in Fig. 2a) is obtained by equating the vertical component of point  $\mathbf{P}$  to the half the height of cylinder  $i$  and solving for  $\theta$ :

$$P_z = \frac{1}{2} L_i \quad (\text{A5})$$

Substituting the  $z$  component of point  $\mathbf{P}$  in the previous equation and solving for  $\theta$  and noting that the  $z$  component of vector  $\mathbf{u}$  is always zero in Eq. (A2).

$$\theta = \sin^{-1} \left( \frac{\frac{1}{2} L_i - C_z}{R_j v_z} \right) \quad (\text{A6})$$

## References

1. Kodam, M., Bharadwaj, R., Curtis, J., Hancock, B., Wassgren, C.: Cylindrical object contact detection for use in discrete element

- method simulations. Part I: contact detection algorithms. *Chem. Eng. Sci.* **65**, 5852–5862 (2010)
2. Guo, Y., Wassgren, C., Ketterhagen, W., Hancock, B., Curtis, J.: Some computational considerations associated with discrete element modeling of cylindrical particles. *Powder Technol.* **228**, 193–198 (2012)
  3. McGeary, R.K.: Mechanical packing of spherical particles. *J. Am. Ceram. Soc.* **44**, 513–522 (1961)
  4. Scott, G.D., Kilgour, D.M.: The density of random close packing of spheres. *J. Phys. D Appl. Phys.* **2**, 863 (1969)
  5. Ouchiyama, N., Tanaka, T.: Porosity estimation for random packings of spherical particles. *Ind. Eng. Chem. Fundam.* **23**, 490–493 (1984)
  6. Shi, Y., Zhang, Y.: Simulation of random packing of spherical particles with different size distributions. *Appl. Phys. A* **92**, 621–626 (2008)
  7. Stroeven, P., Stroeven, M.: Assessment of packing characteristics by computer simulation. *Cem. Concr. Res.* **29**, 1201–1206 (1999)
  8. Tory, E.M., Church, B.H., Tam, M.K., Ratner, M.: Simulated random packing of equal spheres. *The. Can. J. Chem. Eng.* **51**, 484–493 (1973)
  9. Tulluri, S.S.: Analysis of Random Packing of Uniform Spheres Using the Monte-Carlo Simulation Method. Department of Mechanical Engineering, New Jersey Institute of Technology, New Jersey (2003)
  10. Zou, R.P., Yu, A.B.: Evaluation of the packing characteristics of mono-sized non-spherical particles. *Powder Technol.* **88**, 71–79 (1996)
  11. Williams, S.R., Philipse, A.P.: Random packings of spheres and spherocylinders simulated by mechanical contraction. *Phys. Rev. E* **67**, 051301 (2003)
  12. Donev, A., Cisse, I., Sachs, D., Variano, E.A., Stillinger, F.H., Connelly, R., Torquato, S., Chaikin, P.M.: Improving the density of jammed disordered packings using ellipsoids. *Science* **303**, 990–993 (2004)
  13. Zhou, Z.Y., Zou, R.P., Pinson, D., Yu, A.B.: Dynamic simulation of the packing of ellipsoidal particles. *Ind. Eng. Chem. Res.* **50**, 9787–9798 (2011)
  14. Gan, J.Q., Zhou, Z.Y., Yu, A.B.: DEM simulation on the packing of fine ellipsoids. *Chem. Eng. Sci.* **156**, 64–76 (2016)
  15. Evans, K.E., Ferrar, M.D.: The packing of thick fibres. *J. Phys. D Appl. Phys.* **22**, 354–360 (1989)
  16. Buchalter, B.J., Bradley, R.M.: Orientational order in amorphous packings of ellipsoids. *EPL (Europhys. Lett.)* **26**, 159 (1994)
  17. Nolan, G.T., Kavanagh, P.E.: Random packing of nonspherical particles. *Powder Technol.* **84**, 199–205 (1995)
  18. Gan, J.Q., Zhou, Z.Y., Yu, A.B.: Intertparticle force analysis on the packing of fine ellipsoids. *Powder Technol.* **320**, 610–624 (2017)
  19. Abreu, C.R.A., Tavares, F.W., Castier, M.: Influence of particle shape on the packing and on the segregation of spherocylinders via Monte Carlo simulations. *Powder Technol.* **134**, 167–180 (2003)
  20. Lubachevsky, B.D., Stillinger, F.H.: Geometric properties of random disk packings. *J. Stat. Phys.* **60**, 561–583 (1990)
  21. Donev, A., Torquato, S., Stillinger, F.H.: Neighbor list collision-driven molecular dynamics simulation for nonspherical hard particles. I. Algorithmic details. *J. Comput. Phys.* **202**, 737–764 (2005)
  22. Wouterse, A., Luding, S., Philipse, A.P.: On contact numbers in random rod packings. *Granul. Matter* **11**, 169–177 (2009)
  23. Ferreiro-Córdova, C., van Duijneveldt, J.S.: Random Packing of Hard Spherocylinders. *J. Chem. Eng. Data* **59**, 3055–3060 (2014)
  24. Jia, X., Gan, M., Williams, R.A., Rhodes, D.: Validation of a digital packing algorithm in predicting powder packing densities. *Powder Technol.* **174**, 10–13 (2007)
  25. Meng, L., Jiao, Y., Li, S.: Maximally dense random packings of spherocylinders. *Powder Technol.* **292**, 176–185 (2016)
  26. Zhao, J., Li, S., Zou, R., Yu, A.: Dense random packings of spherocylinders. *Soft Matter* **8**, 1003–1009 (2012)
  27. Silbert, L.E.: Jamming of frictional spheres and random loose packing. *Soft Matter* **6**, 2918–2924 (2010)
  28. Delaney, G.W., Hilton, J.E., Cleary, P.W.: Defining random loose packing for nonspherical grains. *Phys. Rev. E Stat. Nonlinear Soft Matter Phys.* **83**, 051305 (2011)
  29. Kyrlyuk, A.V., Wouterse, A., Philipse, A.P.: Random Packings of rod-sphere mixtures simulated by mechanical contraction. *AIP Conf. Proc.* **1145**, 211–214 (2009)
  30. Wouterse, A., Williams, S.R., Philipse, A.P.: Effect of particle shape on the density and microstructure of random packings. *J. Phys. Condens. Matter* **19**, 406215 (2007)
  31. Lu, G., Third, J.R., Müller, C.R.: Critical assessment of two approaches for evaluating contacts between super-quadric shaped particles in DEM simulations. *Chem. Eng. Sci.* **78**, 226–235 (2012)
  32. Zhong, W.Q., Zhang, Y., Jin, B.S., Zhang, M.Y.: Discrete element method simulation of cylinder-shaped particle flow in a gas-solid fluidized bed. *Chem. Eng. Technol.* **32**, 386–391 (2009)
  33. Ren, B., Zhong, W., Jiang, X., Jin, B., Yuan, Z.: Numerical simulation of spouting of cylindroid particles in a spouted bed. *Can. J. Chem. Eng.* **92**, 928–934 (2014)
  34. Tangri, H., Guo, Y., Curtis, J.S.: Packing of cylindrical particles: DEM simulations and experimental measurements. *Powder Technol.* **317**, 72–82 (2017)
  35. Qian, Q., Wang, L., An, X., Wu, Y., Wang, J., Zhao, H., Yang, X.: DEM simulation on the vibrated packing densification of mono-sized equilateral cylindrical particles. *Powder Technol.* **325**, 151–160 (2018)
  36. Wellmann, C., Lillie, C., Wriggers, P.: A contact detection algorithm for superellipsoids based on the common-normal concept. *Eng. Comput.* **25**, 432–442 (2008)
  37. Delaney, G.W., Hilton, J.E., Cleary, P.W., Miller, C.: The role of inter-grain friction in determining the mechanical and structural properties of superellipsoid packings. *AIP Conf. Proc.* **1542**, 361–364 (2013)
  38. Dong, K.J., Wang, C.C., Yu, A.B.: A novel method based on orientation discretization for discrete element modeling of non-spherical particles. *Chem. Eng. Sci.* **126**, 500–516 (2015)
  39. Brilliantov, N.V., Pöschel, T.: Rolling friction of a viscous sphere on a hard plane. *Europhys. Lett.* **42**, 511–516 (1998)
  40. Doraia, F., Rolland, M., Wachs, A., Marcoux, M., Climent, E.: Packing fixed bed reactors with cylinders: influence of particle length distribution. *Proc. Eng.* **42**, 1335–1345 (2012)
  41. Tsuji, Y., Tanaka, T., Ishida, T.: Lagrangian numerical simulation of plug flow of cohesionless particles in a horizontal pipe. *Powder Technol.* **71**, 239–250 (1992)
  42. Guo, Y., Wassgren, C., Ketterhagen, W., Hancock, B., James, B., Curtis, J.: A numerical study of granular shear flows of rod-like particles using the discrete element method. *J. Fluid Mech.* **713**, 1–26 (2012)
  43. Vega, C., Lago, S.: A fast algorithm to evaluate the shortest distance between rods. *Comput. Chem.* **18**, 55–59 (1994)
  44. Rahman, A., Stillinger, F.H.: Molecular dynamics study of liquid water. *J. Chem. Phys.* **55**, 3336–3359 (1971)
  45. Gary, G.H.: A rational approach to drag prediction of spherical and nonspherical particles. *Powder Technol.* **77**, 143–152 (1993)
  46. Evans, D.J., Murad, S.: Singularity free algorithm for molecular dynamics simulation of rigid polyatomics. *Mol. Phys.* **34**, 327–331 (1977)
  47. Džugys, A., Peters, B.: An approach to simulate the motion of spherical and non-spherical fuel particles in combustion chambers. *Granul. Matter* **3**, 231–266 (2001)

48. Goldstein, H., Poole, C.P., Safko, J.L.: *Classical Mechanics*. Addison-Wesley Publishing Company, Boston (1980)
49. Lu, G., Third, J.R., Müller, C.R.: Discrete element models for non-spherical particle systems: from theoretical developments to applications. *Chem. Eng. Sci.* **127**, 425–465 (2015)
50. Gan, J.Q., Zhou, Z.Y., Yu, A.B.: A GPU-based DEM approach for modelling of particulate systems. *Powder Technol.* **301**, 1172–1182 (2016)
51. Blaak, R., Frenkel, D., Mulder, B.M.: Do cylinders exhibit a cubatic phase? *J. Chem. Phys.* **110**, 11652–11659 (1999)
52. Alan, W., Stephen, R.W., Albert, P.P.: Effect of particle shape on the density and microstructure of random packings. *J. Phys.: Condens. Matter* **19**, 406215 (2007)
53. Benyahia, F.: On the global and local structural properties of packed beds of nonequilateral cylindrical particles. *Part. Sci. Technol.* **14**, 221–237 (1996)
54. Delaney, G.W., Cleary, P.W.: The packing properties of superellipsoids. *EPL (Europhys. Lett.)* **89**, 34002 (2010)
55. Yang, R.Y., Zou, R.P., Yu, A.B.: Effect of material properties on the packing of fine particles. *J. Appl. Phys.* **94**, 3025–3034 (2003)
56. Adler, P.M., Thovert, J.-F., Mourzenko, V.V.: *Fractured Porous Media*. OUP Oxford, Oxford (2013)
57. Onsager, L.: The effects of shape on the interaction of colloidal particles. *Ann. N. Y. Acad. Sci.* **51**, 627–659 (1949)
58. Leslie, F.M., Demus, D., Goodby, J., Gray, G.W., Spiess, H.W., Vill, V.: *Theory of the Liquid Crystalline State, Physical Properties of Liquid Crystals*, pp. 25–86. Wiley, Hoboken (2007)
59. Lekkerkerker, H.N.W., Tuinier, R.: *Colloids and the Depletion Interaction, Lecture Notes in Physics*, pp. 188 (2011)
60. Philipse, A.P.: The random contact equation and its implications for (colloidal) rods in packings, suspensions, and anisotropic powders. *Langmuir* **12**, 1127–1133 (1996)
61. Blouwolf, J., Fraden, S.: The coordination number of granular cylinders. *Europhys. Lett. (EPL)* **76**, 1095–1101 (2006)
62. Somfai, E., van Hecke, M., Ellenbroek, W.G., Shundyak, K., van Saarloos, W.: Critical and noncritical jamming of frictional grains. *Phys. Rev. E* **75**, 020301 (2007)
63. Alexander, S.: Amorphous solids: their structure, lattice dynamics and elasticity. *Phys. Rep.* **296**, 65–236 (1998)
64. Aste, T., Saadatfar, M., Sakellariou, A., Senden, T.: Investigating the geometrical structure of disordered sphere packings. *Physica A* **339**, 16–23 (2004)
65. Delaney, G.W., Hilton, J.E., Cleary, P.W.: Defining random loose packing for nonspherical grains. *Phys. Rev. E* **83**, 051305 (2011)
66. Qian, Q., An, X., Zhao, H., Dong, K., Yang, X.: Numerical investigations on random close packings of cylindrical particles with different aspect ratios. *Powder Technol.* **343**, 79–86 (2019)
67. Eberly, D.H.: *3D Game Engine Design: A Practical Approach to Real-Time Computer Graphics*. Morgan Kaufmann, London (2001)

**Publisher's Note** Springer Nature remains neutral with regard to jurisdictional claims in published maps and institutional affiliations.